Gradient Nonlinear Pancharatnam-Berry Metasurfaces

Mykhailo Tymchenko, J. Sebastian Gomez-Diaz, Jongwon Lee, Nishant Nookala,
Mikhail A. Belkin, and Andrea Alù[*]

Department of Electrical and Computer Engineering, The University of Texas at Austin, Austin, Texas 78701, USA

We apply the Pancharatnam-Berry phase approach to plasmonic metasurfaces loaded by highly nonlinear multiquantum-well substrates, establishing a platform to control the nonlinear wave front at will based on giant localized nonlinear effects. We apply this approach to design flat nonlinear metasurfaces for efficient second-harmonic radiation, including beam steering, focusing, and polarization manipulation. Our findings open a new direction for nonlinear optics, in which phase matching issues are relaxed, and an unprecedented level of local wave front control is achieved over thin devices with giant nonlinear responses.

Artificially engineered metasurfaces have recently attracted a great deal of interest due to their ability to provide a large degree of control over the local amplitude, phase, and polarization of local fields, leading to many exciting advances in science and technology [1,2]. Conventional optical devices are based on the naturally weak interactions of light with matter, implying that volumetric effects dominate their optical response. Metasurfaces provide an elegant way to overcome these constraints, by manipulating the local field with suitably engineered inclusions that can enhance the local interaction with light, and pattern it in the desired way over subwavelength distances. Artificially engineered metasurfaces have for the most part been limited to their linear operation to date, with numerous applications such as wave front engineering [1–4], information processing and analog computations [5], spin-orbit manipulation [6], and three-dimensional holography [7], among many others. Artificially engineered metasurfaces have started to make their way into nonlinear optics, where they hold a great promise to reduce the size and dimensionality of current devices, relax issues associated with phase matching requirements [8,9], and boost the nonlinear response [10,11].

Recently, planar ultrathin nonlinear metasurfaces based on the strong coupling of plasmonic resonances with intersubband transitions of multiquantum-well (MQW) semiconductor heterostructures have been shown to produce nonlinear responses that are orders of magnitude larger than natural nonlinear crystals with similar thicknesses [10,11]. MQW heterostructures are known to provide one of the largest nonlinear responses in condensed matter; however, they respond only to electric fields oriented normally to the semiconductor layers [12–18]. This problem was successfully addressed by employing properly designed plasmonic structures that support highly confined resonances at pump and generated frequencies, efficiently coupling the impinging beam to electric field components perpendicular to the semiconductor layers. The giant level of nonlinearities

experimentally observed in these systems opens a new paradigm in nonlinear optics, because they can engage very large nonlinear responses in deeply subwavelength volumes, relaxing the necessity for phase matching, and providing a significant nonlinear response in a confined pixel. This feature ideally lends itself to the possibility of creating metasurfaces able to control the generated nonlinear fields by gradually varying their local phase and amplitude with subwavelength resolution, allowing the use of reflectarray concepts for wave front engineering of the nonlinear generated beam [1,19,20].

In the realm of linear metasurfaces, there have been several approaches to controlling the amplitude and phase of the transmitted wave front, such as locally changing the size of metallic inclusions, or the apex angle of *V*-shaped nanoantennas, or placing metallic particles in elaborate periodic and aperiodic arrangements, to name a few [1]. Another approach is to employ suitably designed optical elements based on the Pancharatnam-Berry (PB) phase concept (PB optical elements), which introduce a geometrical phase difference between transmitted (or reflected) waves based on their geometry and orientation [21,22]. It has been shown that flat metasurfaces consisting of PB optical elements can efficiently tailor the local transmitted or reflected wave by gradually varying their local orientation from cell to cell, thus enabling wide wave front engineering capabilities over a flat platform [23–25]. In this approach, the inclusions need to be accurately designed to ensure proper coupling with the polarization of interest, and to minimize other diffraction effects.

Here, we extend the concept of PB-phase optical elements to the nonlinear regime, and more specifically to MQW-based nonlinear plasmonic metasurfaces, in order to tailor at will the spatial phase distribution of their efficient second harmonic (SH) radiation [10]. Since these giant nonlinear effects are very sensitive to variations in the local resonances of the metasurface, the PB phase

approach becomes an ideal tool to achieve full phase control and at the same time ensures a nearly uniform, giant nonlinear response across the metasurface, based on a single suitably designed PB element that gradually changes its orientation from cell to cell. In addition, our numerical analysis (see [26]) provides an ideal tool to compute both the *amplitude* and *phase* of the emerging SH fields, irrespectively of the resonator design or the nonlinear material employed. This allows the fast design of nonlinear plasmonic metasurfaces with advanced functionalities such as light bending or focusing, while simultaneously providing conversion efficiencies several orders of magnitude larger than any other planar nonlinear configuration [10]. Very recent attempts in this direction [31,32], of which we were unaware at the time of submission, have indeed shown that the concept of gradient metasurfaces can be applied to nonlinear optics. In the following, we apply this concept to multiquantum-well loaded metasurfaces, enabling large conversion efficiency and full control of the phase and amplitude of the generated nonlinear beams with subwavelength resolution.

The general concept of the proposed nonlinear PB metasurface is illustrated in Fig. 1. A thin MQW substrate with layers grown in the x-y plane is sandwiched between an array of suitably designed plasmonic resonators and a metallic ground plane. The incident beam propagates along the z direction, and the metasurface operates in reflection. Each element is designed to ensure giant nonlinear response, similar to [11], and more specifically large second-harmonic conversion efficiency, but at the same time to have a subwavelength footprint. In addition, here we rotate each element of the surface to acquire the desired local geometrical phase for circularly polarized incidence.

Assuming that the coupling between neighboring elements is weak, we can describe the optical response of each element using its effective local nonlinear transverse
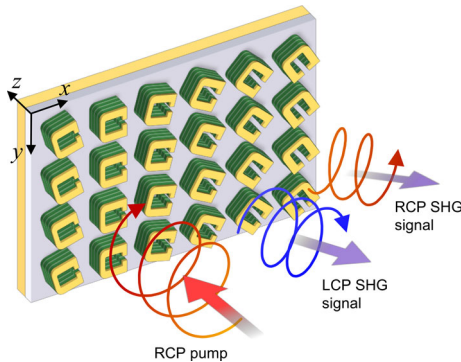

FIG. 1 (color online). A sketch of the proposed PB nonlinear metasurface with a phase gradient in the x direction. The MQW blocks are sandwiched between U-shaped gold resonators and a metallic ground plane. The incident circular polarized wave at ω generates simultaneously RHCP and LHCP nonlinear waves at 2ω.

susceptibility tensor $\overset{\leftrightarrow}{\chi}^{(2)\mathrm{eff}}$, which relates the induced nonlinear transverse polarization density averaged over the volume of the element at frequency 2ω to the transverse incident field at ω [10]. In order to apply the PB phase approach, we recast this tensor in a $\chi^{(2)}_{zzz}$ circular polarization (CP) basis as $\chi^{(2)\mathrm{eff}}_{\alpha\beta\gamma}$, where α, β, and γ can be R or L, corresponding to right-handed (RHCP) and left-handed (LHCP) circularly polarized fields, respectively [26]. Once this effective susceptibility tensor is known, the averaged transverse nonlinear surface currents induced on the metasurface can be readily obtained. Note that we neglect the z-polarized contribution to these currents, which may become relevant for radiation significantly away from broadside (see [26] for the validation of this assumption). For the sake of simplicity, we assume here that only one circularly polarized wave is incident at a time, so that $\gamma = \beta$ always holds. It can be shown that each PB element, rotated as $\varphi(x, y)$ across the surface, when illuminated by a LHCP incident wave $E^\omega_{L(\mathrm{inc})}$ at normal incidence, generates an effective nonlinear transverse surface current that can be split into LHCP and RHCP components denoted as $K^{2\omega}_{L(L)}$ and $K^{2\omega}_{R(L)}$, with spatial variation analytically given by [26]

$$K^{2\omega}_{L(L)}(x, y) = 2\omega\varepsilon_0 h\chi^{(2)\mathrm{eff}}_{LLL}[E^\omega_{L(\mathrm{inc})}]^2 \exp[i3\varphi(x, y)], \quad (1a)$$

$$K^{2\omega}_{R(L)}(x, y) = 2\omega\varepsilon_0 h\chi^{(2)\mathrm{eff}}_{RLL}[E^\omega_{L(\mathrm{inc})}]^2 \exp[i\varphi(x, y)], \quad (1b)$$

where h is the height of the MQW layer. Similar expressions for a RHCP impinging wave $E^\omega_{R(\mathrm{inc})}$ possess the opposite dependence on the local orientation $\varphi(x, y)$, as detailed in [26]. In Eq. (1) we have taken into account that, for a given metasurface configuration, the radiated waves propagate in the direction opposite to the incident wave, and therefore have a reversed circular polarization basis. Remarkably, and differently from the conventional PB phase approach, no optimization of the coupling efficiency to different polarization mechanisms is necessary in this nonlinear operation, and Eqs. (1a) and (1b) always apply. The design of PB elements can therefore be focused on maximally enhancing the nonlinear process of interest to realize giant nonlinear response, and once the optimal inclusion is selected, it simply needs to be rotated gradually along the surface. In addition, for each circularly polarized normally incident wave, the nonlinear output is automatically split into pure circularly polarized components, with different patterning depending only on the local orientation of the inclusions on the surface.

In order to demonstrate the aforementioned concepts, we first design an optimized unit cell to enhance local second-harmonic generation, and then we apply this design to realize PB metasurfaces with tailored nonlinear wave fronts. The optimized cell consists of a U-shaped split-ring plasmonic resonator [see Fig. 2(a)], and follows the

general requirements determined in [10], i.e., (i) locally enhancing the field at resonance, (ii) supporting resonances with overlapping modal distributions at fundamental and second-harmonic frequency, and (iii) efficiently converting the transversely impinging and outgoing electric fields into locally enhanced vertical fields. In addition, the PB approach imposes additional requirements to the unit-cell design, including that (iv) it must sit on a subwavelength footprint, (v) it must allow rotation within the same footprint, and (vi) it must ensure weak coupling between neighboring cells. In our design, we employ the same MQW heterostructure as in [10], with thickness $h = 500$ nm and $\chi^{(2)}_{zzz} = 54$ nm V^{-1} at 37 THz, and we etch the MQW layer around the resonator to reduce the coupling between adjacent PB elements. The size of the plasmonic resonator and unit cell, specified in Fig. 2(b), were optimized to achieve overlapping resonances at fundamental and second-harmonic frequencies, 37 THz ($\lambda_\omega = 8$ μm) and 74 THz ($\lambda_{2\omega} = 4$ μm), respectively. Figure 2(c) shows the spatial distribution of the normalized z component of the electric field near the plasmonic resonator at the two frequencies. At the fundamental frequency ω the structure is efficiently excited by a y-polarized wave, whereas at 2ω the structure responds to x-polarized fields, as confirmed in the absorption spectrum shown in Fig. 2(d). Our numerical simulations [26] confirm a peak conversion efficiency before saturation above $(2 \times 10^{-4})\%$, similar to the one experimentally obtained in [10] and several orders of magnitude larger than those found in planar nonlinear metasurfaces based on conventional optical materials for similar levels of intensities.
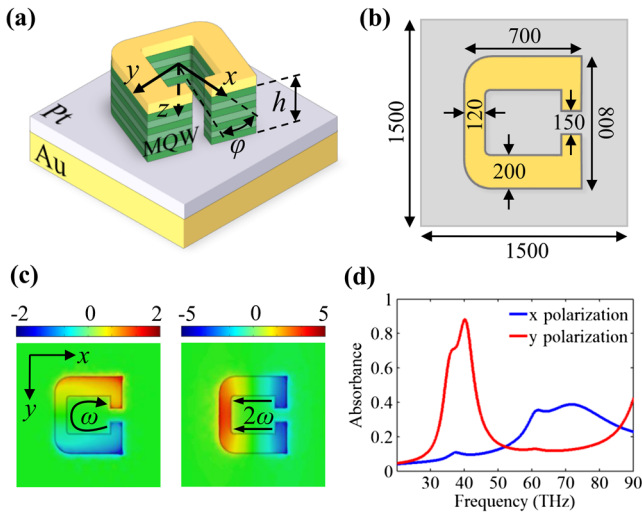

FIG. 2 (color online). (a) Geometry of a PB metasurface element. (b) Dimensions (in nm) of the gold plasmonic resonator. The MQW layer is etched around the resonator. (c) Spatial distribution of the normalized z component of the field at the top of the MQW layer at the fundamental and second-harmonic frequencies, E_z^ω and $E_z^{2\omega}$, respectively. (d) Simulated absorption spectrum for different polarizations.

The first example of nonlinear PB metasurface operation is aimed at steering the generated beams towards specific directions. To this goal, the metasurface should provide a linear phase gradient along one direction at the second-harmonic frequency 2ω, realizing a periodic superlattice composed of supercells with period $L = Nd$, where d is the size of each unit cell, and N is the number of elements required to complete a full turn around the z axis, i.e., from $\varphi = 0$ to $\varphi = 360°$. We choose the unit cell size $d = 1.5$ μm [Fig. 2(b)] with an angular rotation step $\Delta\varphi = 15°$ between neighboring cells, chosen to be small enough in order to limit unwanted phase variations that may break the assumptions at the basis of Eq. (1). The supercell therefore contains $N = 24$ unit cells, corresponding to $L = 36$ μm. From basic reflectarray theory [19] and Eqs. (1a) and (1b), it follows that for a LHCP wave normally incident on the surface at ω, the waves radiated by the LHCP and RHCP currents at 2ω will propagate at angles $\theta_{L(L)} = -\arcsin[(3\Delta\varphi/360°)\lambda_{2\omega}/d]$ and $\theta_{R(L)} = -\arcsin[(\Delta\varphi/360°)\lambda_{2\omega}/d]$, which for our geometry are $-20°$ and $-7°$ with respect to the $-z$ direction, respectively. Analogously, from Eqs. (3a) and (3b) it follows that under RHCP incidence the metasurface supports RHCP and LHCP currents radiating at $\theta_{R(R)} = -\theta_{L(L)}$ and $\theta_{L(R)} = -\theta_{R(L)}$, respectively. It should be noticed that, while the induced currents are purely CP as predicted by Eq. (1), the radiated waves in general are only partially CP, as they travel at an angle from the normal. However, for radiation angles relatively close to the normal, as in the cases considered here, the radiated waves are circularly polarized with very good approximation [26]. Figure 3(a) shows the analytically and numerically calculated phases of the effective induced surface currents $K^{2\omega}_{\alpha(L)}(x)$ under LHCP illumination, as a function of position along the superlattice period L (see [26] for a description of computational methods). The corresponding variation of the magnitude of the tensor elements $\chi^{(2)\text{eff}}_{\alpha\beta\beta}$ normalized to $\chi^{(2)}_{zzz}$ is shown in Fig. 3(b), reporting average values $\langle\chi^{(2)\text{eff}}_{RLL}\rangle = 11$ nm V^{-1}, $\langle\chi^{(2)\text{eff}}_{LLL}\rangle = 19$ nm V^{-1}, which are of the same order as the results reported in [10], confirming that the phase control functionality does not affect the overall high efficiency of the nonlinear process (see [26] for an extended discussion on conversion efficiency). The slight discrepancy between theoretical and numerical results is due to the small differences in the coupling between adjacent resonators as a function of their orientation. Figure 3(c) shows the simulated spatial distribution of $E_y^{2\omega}$ above the metasurface illuminated by a 30 μm-wide LHCP Gaussian beam. The simulation results confirm that the radiated field cleanly splits into two separate beams with opposite handedness and different directions, as predicted by our theory. In our design, since $\chi^{(2)\text{eff}}_{LLL} > \chi^{(2)\text{eff}}_{RLL}$, the LHCP beam has larger amplitude than the RHCP one, which is clearly observed in Fig. 3(d). Proper optimization of the unit cell may provide similar intensities, or completely
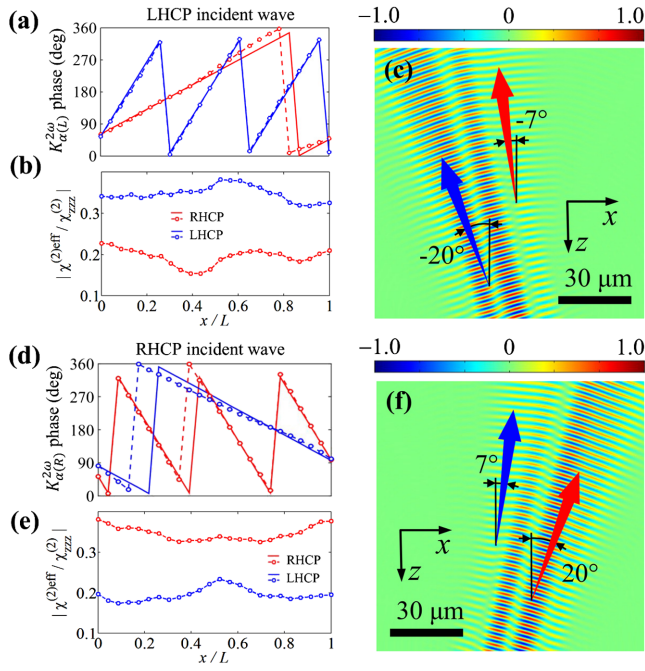
FIG. 3 (color online). Analytical and numerical results for a flat nonlinear metasurface with a linear variation of the PB elements' orientation along the x axis, considering an angular step $\Delta\varphi$ of 15°. (a) Phases of RHCP and LHCP components of the effective nonlinear surface current generated on the metasurface by a LHCP plane wave at normal incidence at ω. Analytical results are shown with solid lines, dashed lines with markers show the corresponding numerical results. (b) Magnitude of the $\overset{\leftrightarrow}{\chi}^{(2)\mathrm{eff}}$ elements computed for each cell, normalized by $\chi_{zzz}^{(2)}$. (c) Spatial distribution of the $E_y^{2\omega}$ component of the radiated field above the metasurface illuminated by a 30 μm-wide LHCP Gaussian beam (the incident field is not shown). (d)–(f) Same as in (a)–(c), but for an RHCP impinging wave at normal incidence.

suppress one of the two beams, depending on the application of interest. Figure 3(d)–3(f) show the results for the same PB metasurface under RHCP excitation. As mentioned above, in this case the phase shifts and directions of the beams are opposite. The average values of the nonlinear susceptibility tensor elements are the same, namely $\langle\chi_{RLL}^{(2)\mathrm{eff}}\rangle = \langle\chi_{LRR}^{(2)\mathrm{eff}}\rangle$ and $\langle\chi_{LLL}^{(2)\mathrm{eff}}\rangle = \langle\chi_{RRR}^{(2)\mathrm{eff}}\rangle$. If we excite at oblique incidence, the transverse momentum imprinted on the PB currents is added to the momentum of the impinging excitation, allowing continuous steering of the nonlinear beams. For steeper incidence and radiation angles, additional contributions from vertically polarized nonlinear currents may be expected, depending on the metasurface design, which has been neglected here. We verify and further discuss in [26] how this approximation holds very well for the examples considered in this Letter.

Another classical example of linear metasurface operation is focusing the radiated field in the near field of the metasurface. Since the right- and left-handed polarized components of the second-harmonic field possess different
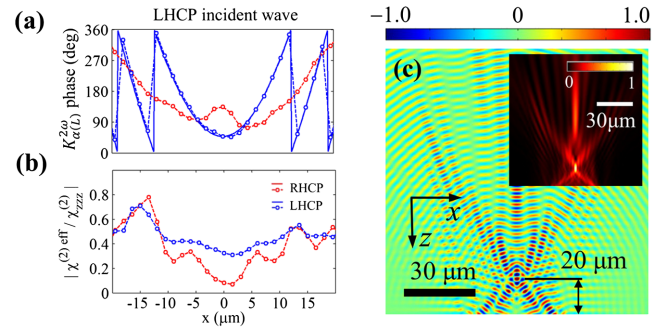

FIG. 4 (color online). Focusing the LHCP nonlinear radiation 20 μm above the metasurface. The structure is illuminated by LHCP normally impinging waves. (a) Analytically (solid lines) and numerically (dashed lines with markers) computed phases of RHCP and LHCP components of the effective nonlinear current induced on the metasurface by a LHCP incident plane wave at ω. (b) Local magnitude of the $\overset{\leftrightarrow}{\chi}^{(2)\mathrm{eff}}$ elements normalized by $\chi_{zzz}^{(2)}$. (c) Spatial distribution of the $E_y^{2\omega}$ component of the radiated field above the metasurface illuminated by a 30 μm-wide LHCP Gaussian beam (not shown). The inset shows the corresponding spatial distribution of the energy density.

phase dependence on the local PB element orientation, their focusing requirements would be different. Our design is aimed at focusing the LHCP component of the generated beam at $f = 20$ μm above the nonlinear metasurface under LHCP normal incidence. The required spatial variation of the PB elements orientation is not periodic any longer, but it has a quadratic dependence $\varphi(x) = 360°[(x^2 + f^2)^{1/2} - f]/3\lambda_{2\omega}$ [1]. Figure 4(a) shows the analytical and numerical phase of the induced surface currents $K_{\alpha(L)}^{2\omega}(x)$. The magnitude of the corresponding $\overset{\leftrightarrow}{\chi}^{(2)\mathrm{eff}}$ elements varies from cell to cell slightly more than in the previous case, as can be seen in Fig. 4(b), averaging around $\langle\chi_{LLL}^{(2)\mathrm{eff}}\rangle = 24$ nm V^{-1}, $\langle\chi_{RLL}^{(2)\mathrm{eff}}\rangle = 22$ nm V^{-1}. Figure 4(c) shows the spatial distribution of $E_y^{2\omega}$ for the same 30 μm LHCP impinging beam incident at normal incidence, as in the first example. The inset shows the corresponding spatial distribution of the time-averaged energy density of the radiated field. Our results confirm that nearly perfect focusing of the radiated LHCP wave is achieved at the desired point. A change of incident polarization to RHCP will result in strong nonlinear radiation defocusing [26].

In conclusion, we have shown that the PB phase approach extended to nonlinear optics constitutes a powerful tool to engineer gradient metasurfaces with giant nonlinear response, greatly enriching their functionality and opening fascinating prospects for wave front engineering of nonlinear frequency generation, supported by the absence of phase matching requirements. While this approach cannot be considered a direct extension of the linear PB approach, since it cannot be any longer mapped over a single Poincaré sphere due to the frequency transformation, it allows continuous control of the phase

imparted to the generated nonlinear beam through geometrical rotations. Importantly, and different from the linear PB approach, the wave front engineering capabilities of such metasurfaces do not require sacrificing their performance, since the nonlinear response is inherently associated to their subwavelength footprint. Our approach can be easily extended to other nonlinear phenomena, such as third harmonic, sum and difference frequency generation, phase conjugation, and more. In addition, the proposed concept can also be applied to nonlinear metasurfaces with a dielectric substrate that operate in transmission.

---

*alu@mail.utexas.edu

[1] N. Yu and F. Capasso, Nat. Mater. **13**, 139 (2014).

[2] A. Kildishev, Alexander V. Boltasseva, and V. M. Shalaev, Science **339**, 1232009 (2013).

[3] C. L. Holloway, E. F. Kuester, J. A. Gordon, J. O'Hara, J. Booth, and D. R. Smith, IEEE Antennas Propag. Mag. **54**, 10 (2012).

[4] N. Yu, P. Genevet, M. A. Kats, F. Aieta, J.-P. Tetienne, F. Capasso, and Z. Gaburro, Science **334**, 333 (2011).

[5] A. Silva, F. Monticone, G. Castaldi, V. Galdi, A. Alù, and N. Engheta, Science **343**, 160 (2014).

[6] G. Li, M. Kang, S. Chen, S. Zhang, E. Y. B. Pun, K. W. Cheah, and J. Li, Nano Lett. **13**, 4148 (2013).

[7] L. Huang, X. Chen, H. Mühlenbernd, H. Zhang, S. Chen, B. Bai, Q. Tan, G. Jin, K.-W. Cheah, C.-W. Qiu, J. Li, T. Zentgraf, and S. Zhang, Nat. Commun. **4**, 2808 (2013).

[8] J. A. Armstrong, N. Bloembergen, J. Ducuing, and P. S. Pershan, Phys. Rev. **127**, 1918 (1962).

[9] R. W. Boyd, Nonlinear Optics, 3rd ed. (Academic Press, San Diego, 2008).

[10] J. Lee, M. Tymchenko, C. Argyropoulos, P.-Y. Chen, F. Lu, F. Demmerle, G. Boehm, M.-C. Amann, A. Alù, and M. A. Belkin, Nature (London) **511**, 65 (2014).

[11] S. Campione, A. Benz, M. B. Sinclair, F. Capolino, and I. Brener, Appl. Phys. Lett. **104**, 131104 (2014).

[12] M. M. Fejer, S. J. B. Yoo, R. L. Byer, A. Harwit, and J. S. Harris, Jr., Phys. Rev. Lett. **62**, 1041 (1989).

[13] E. Rosencher, P. Bois, J. Nagle, and S. Delattre, Electron. Lett. **25**, 1063 (1989).

[14] F. Capasso, C. Sirtori, and A. Y. Cho, IEEE J. Quantum Electron. **30**, 1313 (1994).

[15] E. Rosencher, A. Fiore, B. Vinter, V. Berger, P. Bois, and J. Nagle, Science **271**, 168 (1996).

[16] C. Gmachl, A. Belyanin, D. L. Sivco, M. L. Peabody, N. Owschimikow, A. M. Sergent, F. Capasso, and A. Y. Cho, IEEE J. Quantum Electron. **39**, 1345 (2003).

[17] M. A. Belkin, F. Capasso, A. Belyanin, D. L. Sivco, A. Y. Cho, D. C. Oakley, C. J. Vineis, and G. W. Turner, Nat. Photonics **1**, 288 (2007).

[18] K. Vijayraghavan, Y. Jiang, M. Jang, A. Jiang, K. Choutagunta, A. Vizbaras, F. Demmerle, G. Boehm, M. C. Amann, and M. A. Belkin, Nat. Commun. **4**, 2021 (2013).

[19] J. Huang and J. A. Encinar, Reflectarray Antennas (Wiley-IEEE Press, Hoboken, NJ, 2007).

[20] F. Monticone, N. M. Estakhri, and A. Alù, Phys. Rev. Lett. **110**, 203903 (2013).

[21] S. Pancharatnam, Resonance **18**, 387 (2013).

[22] M. V. Berry, J. Mod. Opt. **34**, 1401 (1987).

[23] Z. Bomzon, G. Biener, V. Kleiner, and E. Hasman, Opt. Lett. **27**, 1141 (2002).

[24] G. Biener, A. Niv, V. Kleiner, and E. Hasman, Opt. Lett. **27**, 1875 (2002).

[25] S.-C. Jiang, X. Xiong, Y.-S. Hu, S.-W. Jiang, Y.-H. Hu, D.-H. Xu, R.-W. Peng, and M. Wang, Phys. Rev. B **91**, 125421 (2015).

[26] See Supplemental Material at http://link.aps.org/supplemental/10.1103/PhysRevLett.115.207403, which includes Refs. [27–30] and contains details about theoretical and numerical methods used in the paper, a discussion of saturation and absorption effects, and additional figures.

[27] J. S. Gomez-Diaz, M. Tymchenko, J. Lee, M. A. Belkin, and A. Alù, Phys. Rev. B **92**, 125429 (2015).

[28] C. A. Balanis, Advanced Engineering Electromagnetics, 2 ed. (John Wiley & Sons, Inc., New Jersey, 2012).

[29] CST–Computer Simulation Technology 2015 [https://www.cst.com].

[30] COMSOL 4.4 Multiphysics Modeling Software [https://www.comsol.com].

[31] N. Segal, S. Keren-Zur, N. Hendler, and T. Ellenbogen, Nat. Photonics **9**, 180 (2015).

[32] G. Li, S. Chen, N. Pholchai, B. Reineke, P. W. H. Wong, E. Y. B. Pun, K. W. Cheah, T. Zentgraf, and S. Zhang, Nat. Mater. **14**, 607 (2015).